Modeling and Nonlinear Dynamic Analysis of a Photovoltaic System With Multiple Parallel Branches Based on Simplified Discrete Time Model

Xinyue Geng, Bo Zhang, *Fellow, IEEE*, Dongyuan Qiu, *Senior Member, IEEE*, Yanfeng Chen, *Member, IEEE*, Wenxun Xiao, *Member, IEEE*, and Fan Xie, *Member, IEEE*

***Abstract*—The widely used dc distribution system mainly based on new energy generation consists of multiple power electronic converters in series and parallel. The mutual coupling among these converters can lead to complex nonlinear behavior. It is necessary to build a more accurate mathematical model for identifying a more comprehensive nonlinear behavior of this kind of high-order complex system. Therefore, a double-branch parallel photovoltaic system is taken as the research object in this article, where we carry out accurate modeling and nonlinear dynamic analysis of the system. First, the influence of environmental factors on the output characteristic of the system is considered when modeling the photovoltaic generator. Second, the simplified discrete-time model is introduced in the dynamic model, which not only simplifies the calculation process but also ensures the accuracy of the calculation results, and is suitable for systems with different switching frequencies. Subsequently, the nonlinear behaviors of the system are analyzed in detail by using the constructed model, and the Hopf bifurcations are identified. Through the simulation comparison, the significant advantage in the calculation accuracy of the modeling results is verified. Finally, the effectiveness of the theoretical analysis is further demonstrated through experimental verification.**

***Index Terms*—Discrete-time mapping model, nonlinear behavior, parallel dc–dc converters, photovoltaic (PV) system.**

I. Introduction

With the increasingly severe energy crisis and the rapidly developing power industry, dc distributed systems, mainly based on new energy generation, will become the basic support link for the future energy Internet [1], [2], [3]. Nowadays, photovoltaic (PV) power generation technology is widely used due to its advantages such as low emissions and easy maintenance. Usually, dc distribution systems primarily powered by new energy sources such as PV can output to a common dc bus or dc load through *m* parallel branches, each of which consists of a PV module and a boost dc–dc converter [4], as shown in Fig. 1. This PV system with multiple parallel dc–dc converters is a nonlinear system, so, there are various nonlinear behaviors [5], [6].

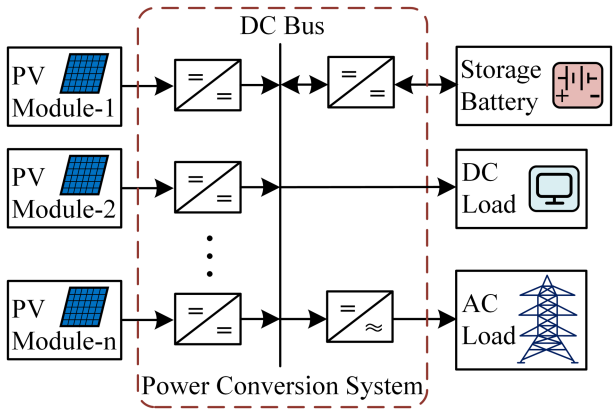

Fig. 1. Model of a PV-based DC distribution system.

Due to the existence of nonlinear behaviors, unreasonable parameter settings of a certain component in the circuit [7], or external conditions affecting the actual power of the system [8], will cause the system to transition from stable operation to instability, thereby increasing the ripple and electromagnetic interference of the circuit, which has a significant impact on system reliability. More importantly, for a PV system with multiple parallel branches as shown in Fig. 1, the complexity of its topology and the coupling of its output terminals will have more unpredictable impacts on system stability [9], [10], [11]. Therefore, there is an urgent need for more reliable nonlinear behavior analysis to guide the parameter design of multiple parallel branches PV systems.

The prerequisite for obtaining reliable nonlinear behaviors is to establish an accurate system dynamic model. Currently, a large number of studies about more effective modeling methods have been proposed. The state-space average (SSA) model was used to study the nonlinear dynamic behavior of a single boost converter in PV systems [12], [13], [14]. However, SSA ignored high-frequency characteristics, so it can only predict slow-scale instability with low accuracy. A more accurate discrete-time mapping model (DMM) was established for the single PV system [15], [16], [17], but in practical applications, the PV

Manuscript received 7 December 2023; revised 3 March 2024; accepted 4 April 2024. Date of publication 15 April 2024; date of current version 20 June 2024. This work was supported by the National Natural Science Foundation of China under Grant U2166601. Recommended for publication by Associate Editor F.D. Freijedo. *(Corresponding author: Fan Xie.)*

The authors are with the School of Electric Power, South China University of Technology, Guangzhou 510640, China (e-mail: 202121016667@mail.scut.edu.cn; epbzhang@scut.edu.cn; epdyqiu@scut.edu.cn; eeyfchen@scut.edu.cn; xiaowx@scut.edu.cn; epfxie@scut.edu.cn).

Color versions of one or more figures in this article are available at https://doi.org/10.1109/TPEL.2024.3388577.

Digital Object Identifier 10.1109/TPEL.2024.3388577

system generally does not exist in a separate form, and this analysis ignores the influence of subsystem coupling. DMM was applied to hybrid energy storage systems with parallel branches in [18], but the modeling process is very complex. When the system has more branches, DMM is difficult to apply. Impedance criteria were used to model the dc–dc converter system in series or parallel [19], [20], [21], but this method is based on SSA, making it difficult to ensure the accuracy of the results [22]. In addition, multibranch systems were analyzed using the describing function method [23], [24], but the calculation process was complex and the analysis results were incomplete, making it difficult to expand. Moreover, literature [25] pointed out that the different switching frequencies are also one of the factors that need to be considered for complex systems with multiple branches, but this problem cannot be solved effectively by using existing methods. If the current modeling methods are applied to the study of the nonlinear dynamic behavior of multibranch new energy generation systems, it is not only difficult to balance the accuracy of results and the simplicity of calculations, but also the application range is not complete enough. Therefore, the modeling and nonlinear dynamic analysis of new energy generation systems with multiple parallel branches is still a problem that needs to be studied.

Based on the current research status, the stability of a double-branch parallel PV system is studied in this article. To solve the modeling difficulties of multiple parallel branch systems with multiple switching devices, the simplified discrete-time model (DTM) of cascaded dc–dc converters proposed in our previous work [26] is applied to parallel converters. For multiple parallel branches systems, this method can not only reduce computational complexity while ensuring accuracy but also accurately analyze systems with different switching frequencies, effectively solving the problems of traditional methods such as SSA and DMM. Subsequently, the PV panel placement angle and internal control parameters of the system were taken as research objects. To analyze the impact of external conditions and internal parameters on system stability, the stability region was divided to provide design guidance.

The rest of this article is organized as follows. The studied system and its operating principles are explained in Section II. A mathematical model of the PV generator affected by external conditions is provided in Section III. The simplified DTM of the entire system is performed in Section IV. Then, stability analysis based on the studied model is conducted in Section V. The effectiveness of the proposed method is verified through experiments and simulations in Section VI. Finally, Section VII concludes this article.

II. System Description of Parallel Photovoltaic System With Boost Converter

In this article, a double-branch parallel PV system is analyzed. The operation principle will be briefly summarized in this section, and the mathematical models of each part will be detailed in Sections III and IV.

The schematic diagram of the double-branch parallel PV system powered by the PV generator and connected to the load through the boost converters is shown in Fig. 2, where, L_1

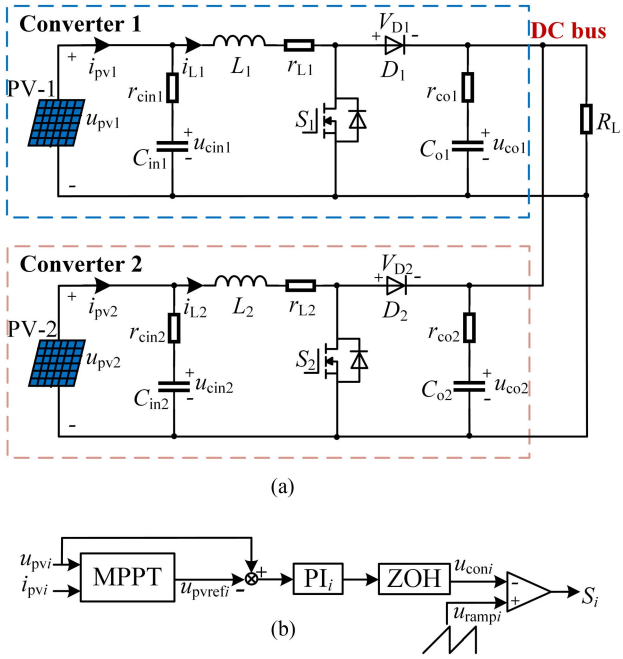

Fig. 2. Circuit diagram of the studied system. (a) Main circuit. (b) Control circuit of the converter i ($i = 1, 2$).

and L_2 are the series inductors of converter 1 and converter 2, respectively. r_{L1} and r_{L2} correspond to the dc resistance (DCR) of the inductor. C_{in1} and C_{in2} and C_{o1} and C_{o2} correspond to the input capacitors and output capacitors of converter 1 and converter 2. r_{cin1} and r_{cin2} and r_{co1} and r_{co2} are the equivalent series resistance of the input capacitors and output capacitors. V_{D1} and V_{D2} are the voltage drop of diodes D_1 and D_2. R_L is the load resistance of the output end. In addition, u_{pv1} and u_{pv2} and i_{pv1} and i_{pv2} correspond to the output voltage and the output currents of PV cells, respectively. i_{L1} and i_{L2} are the inductor currents of the inductors L_1 and L_2, respectively. u_{cin1} and u_{cin2} and u_{co1} and u_{co2} correspond to the capacitor voltage of the capacitors C_{in1} and C_{in2} and C_{o1} and C_{o2}, respectively.

In the PV generation system shown in Fig. 2, two PV cells are connected to the same load through independent boost converters. Between them, the boost converter has two main functions: first, it increases the lower output voltage of the PV cell u_{pv} to a level that matches the local dc bus voltage. The second is to control the output voltage of the PV cell u_{pv} through the switch of the boost converter, to maintain near the maximum power point and continuously output electrical energy [27], [28]. In small household PV systems, the output of the boost converter can be directly connected to the household dc load. Excess electrical energy can also be fed into the local power grid through the dc–ac inverter and the output voltage of the boost converter will also be controlled near the dc bus voltage through the switch of the subsequent dc–ac inverter. To more intuitively reflect the impact of parallel branches on the PV system, this circuit mainly analyzes the bifurcation of the PV system when the output is connected to the dc load.

According to the function of the dc–dc converter in the PV system, the switch S_i of the boost converter i should be controlled by the maximum power point tracking (MPPT). Fig. 2(b) shows

the specific control process: by collecting the output voltage $u_{\mathrm{pv}i}$ and output current $i_{\mathrm{pv}i}$ at both ends of the PV cell, the maximum power point $P_{\mathrm{pvmax}i}$ with the current solar irradiance Ir and temperature T can be estimated by the specific MPPT algorithm, as well as the corresponding voltage $u_{\mathrm{pvmax}i}$ of this point, namely $u_{\mathrm{pvref}i}$ in Fig. 2(b). Then, $u_{\mathrm{pvref}i}$ is compared with the output voltage of PV cell $u_{\mathrm{pv}i}$, and the output voltage of PV cell $u_{\mathrm{pv}i}$ is adjusted to near the maximum power point by reducing the error through the voltage loop. In Fig. 2(b), zero-order holder (ZOH) in the voltage loop is a zero-order holder, which functions to maintain its input signal for one switching period. The reason for adding ZOH is the control circuit needs to use digital control instead of analog control due to the presence of MPPT control. In digital control, the circuit needs to convert the analog signal into a digital signal through ADC sampling, which is usually considered to have a sampling and holding function within one switching period.

III. Mathematical Modeling of the PV Generator

In this section, the mathematical model of the PV generator will be introduced in detail, and the influence of PV panel placement angle on the model will be considered to increase the practicality of the model. Finally, the model is linearized near the maximum power point to facilitate the modeling of the PV generator and its subsequent converter.

A. Nonlinear Model of a PV Generator

PV generator sets have nonlinear characteristics that vary with the external temperature T and solar irradiance Ir, and the most commonly used i–u characteristic equations mainly include the single-diode model [29], [30], the dual-diode model [31], and engineering equivalent mathematical model [32]. When the focus is on analyzing the stability of the entire PV system, most scholars simplify PV cells directly in the form of a constant current source, which is undoubtedly inaccurate [18], [33]. The single-diode model was considered in stability analysis [34], [35], but the influence of external conditions on system stability was ignored. Meanwhile, due to the need for linearization of PV cells near the maximum power point in stability analysis, the conversion process of the single-diode model is very complex. Compared to the single-diode model, the dual-diode model is more accurate, but when applied to stability analysis, the complexity of the model transformation process may affect the uncertainty of the results. The engineering equivalent mathematical model was used in [36] and [37], which simplifies the conversion process and is therefore widely used for stability analysis of PV systems. Therefore, the engineering equivalent mathematical model is adopted and its mathematical expression is as follows:

$$i_{\mathrm{pv}} = I_{\mathrm{SC}}[1 - C_1(e^{u_{\mathrm{pv}}/(C_2U_{\mathrm{OC}})} - 1)]. \tag{1}$$

Among them

$$\begin{cases} C_1 = (1 - \frac{I_{\mathrm{mpp}}}{I_{\mathrm{SC}}})e^{-U_{\mathrm{mpp}}/(C_2U_{\mathrm{OC}})} \\ C_2 = (\frac{U_{\mathrm{mpp}}}{U_{\mathrm{OC}}} - 1)/\ln(1 - \frac{I_{\mathrm{mpp}}}{I_{\mathrm{SC}}}) \end{cases}. \tag{2}$$

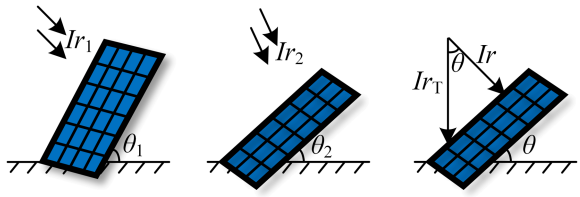

Fig. 3. Schematic diagram of actual solar irradiance affected by solar incidence angle and PV panel angle.

In (2), $U_{\mathrm{OC\_ref}}$ is the open circuit voltage of the PV panel, $I_{\mathrm{SC\_ref}}$ is the short circuit current, $U_{\mathrm{mpp\_ref}}$ and $I_{\mathrm{mpp\_ref}}$, respectively, are the maximum power point voltage and current when the temperature T_{ref} is 25 °C, and the solar irradiance Ir_{ref} is 1000 W/m^2. The above four parameters are all related to external conditions. When the external temperature and solar irradiance are different from the standard test conditions, each parameter in the above formula can be expressed as follows:

$$\begin{cases} U_{\mathrm{OC}} = U_{\mathrm{OC\_ref}}(1 + b\Delta T)(1 + c\Delta Ir) \\ I_{\mathrm{SC}} = I_{\mathrm{SC\_ref}} \cdot \frac{Ir}{Ir_{\mathrm{ref}}}(1 + a\Delta T) \\ U_{\mathrm{mpp}} = U_{\mathrm{mpp\_ref}}(1 + b\Delta T)(1 + c\Delta Ir) \\ I_{\mathrm{mpp}} = I_{\mathrm{mpp\_ref}} \cdot \frac{Ir}{Ir_{\mathrm{ref}}}(1 + a\Delta T) \end{cases}. \tag{3}$$

In (3),$\Delta T = T + k \cdot Ir - T_{\mathrm{ref}}$ and $\Delta Ir = Ir/Ir_{\mathrm{ref}} - 1$, where a is the current temperature coefficient, b is the voltage temperature coefficient, c is the voltage solar irradiance coefficient, T and Ir are the ambient temperature and solar irradiance in the current condition respectively, and k is the temperature coefficient of the PV cell when the solar irradiance changes, using a typical value of 0.3 °C•m^2/W.

B. Effect of Placement Angle on Mathematical Model

In practical applications, the placement angle of PV panels will affect the actual received solar irradiance of PV panels, and the output characteristics of PV cells will be affected to varying degrees. Usually, to ensure the reliable operation of the system, the local geographical conditions and placement angle to be comprehensively considered are necessary when placing the PV panels.

When the angle of the PV panel from the ground is different, the radiation of the solar irradiance on the PV panel will change, this affects the output power of the PV panel. To ignore the influence of geographical conditions, the incident solar irradiance can be set as the vertical plane solar irradiance Ir_{T}. It is not difficult to obtain from Fig. 3(c) that the relationship between the actual received solar irradiance Ir of the PV panel and the vertical plane solar irradiance Ir_{T} is $Ir = Ir_{\mathrm{T}} \cdot \cos\theta$, where θ is the angle of the PV panel. So, ΔIr and ΔT in (3) can be expressed as

$$\begin{cases} \Delta Ir = Ir_{\mathrm{T}} \cdot \cos\theta/Ir_{\mathrm{ref}} - 1 \\ \Delta T = T + k \cdot Ir_{\mathrm{T}} \cdot \cos\theta - T_{\mathrm{ref}} \end{cases}. \tag{4}$$

Substitute (4) into (3) to obtain the actual output values of the PV generator affected by external conditions U_{OC}, I_{SC}, U_{mpp}, and I_{mpp}.

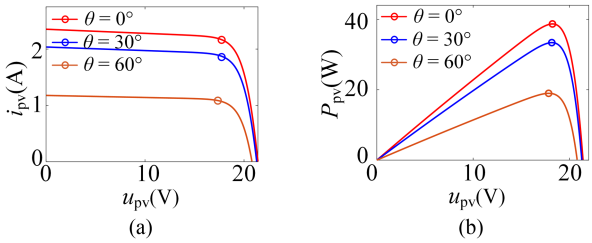

Fig. 4. Output characteristic curve when the placement angle changes. (a) *i–u* curve. (b) *P–u* curve.

As can be seen from Fig. 4, when the PV panel angle θ is different, PV cells will exhibit different *i–u* characteristic curves and corresponding *P–u* characteristic curves, and obtain different maximum power points. With the increase of the PV panel angle θ, the output power $P_{\rm pv}$ of the PV panel will decline, and the corresponding output current $i_{\rm pv}$ and output voltage $u_{\rm pv}$ will also decline. It can be seen that when installing PV panels, the appropriate placement angle should be selected to maximize the solar energy conversion efficiency and stability.

C. Approximate Model Close to the Maximum Power Point

PV generator mainly has three working areas, namely the constant current area, the constant voltage area, and the maximum power point area. In practical application, the PV generator is expected to work in the maximum power point area. To facilitate subsequent analysis, it is considered to extend the nonlinear model of the PV array to the Taylor pole number near the maximum power point and ignore the higher order term. The linear Norton equivalent model can be written as follows:

$$i_{\rm pv} = I_{\rm mpp} + \frac{\partial i_{\rm pv}}{\partial u_{\rm pv}}(u_{\rm pv} - U_{\rm mpp}) \tag{5}$$

where

$$\frac{\partial i_{\rm pv}}{\partial u_{\rm pv}} = -\frac{I_{\rm SC}C_1}{C_2 U_{\rm OC}} e^{U_{\rm mpp}/(C_2 U_{\rm OC})}. \tag{6}$$

It can be seen from (3) that all parameters in (5) and (6) are related to external conditions. Therefore, this method of linearization near extreme points correctly reveals the influence of the nonlinear characteristics of PV generators under different ambient temperatures and light intensities.

IV. Dynamic Modeling of the Studied System

In the actual PV system, the output of the PV cell can always be controlled near the maximum power point by controlling the switch of the converter. Therefore, the mathematical model of a double-branch parallel PV system with MPPT control will be derived in this section. Among them, the steps and application range of the modeling method are summarized in Section IV-A, the dynamic model of the main circuit and control circuit of the studied model is introduced in Section IV-B, and the simplified DTM is used to more accurately derive the model in Section IV-C.

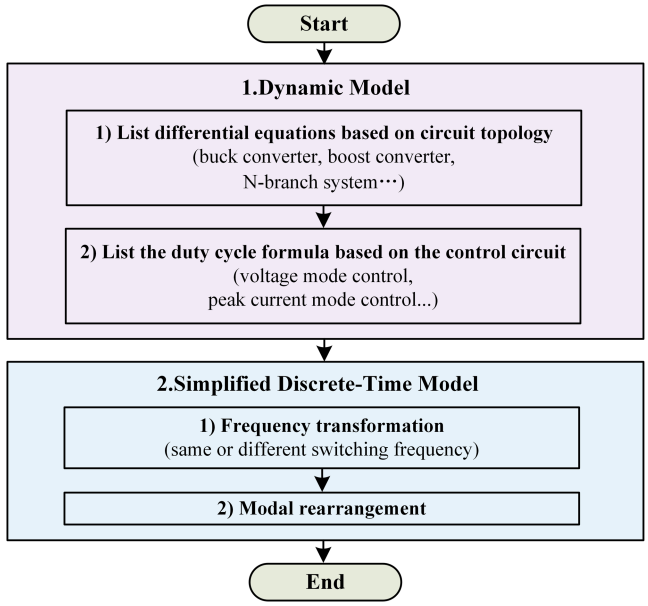

Fig. 5. Flowchart of modeling.

A. Modeling Steps and Model Applicability

The flowchart for establishing the model of the studied system is shown in Fig. 5, modeling the system mainly involves two steps.

1) List the Dynamic Model of the System Based on the Circuit Topology: First, it is necessary to list the differential equations of the main circuit based on Kirchhoff's laws. In this step, the topology of the main circuit can be the buck converter, boost converter, or other dc–dc converters in series and parallel. For example, the system composed of two boost converters in parallel is considered in this article. Second, it is necessary to list the expression for the duty cycle of each power switch in the system. In this step, the control circuit can use common control methods such as voltage mode control, peak current control, average current control, etc.

Establishing a dynamic model is the most common and essential step in modeling dc–dc converters. In this step, the system can be composed of any dc–dc converter in series or parallel, or any control method can be used. Therefore, this has also become the main reason for the universality of the model in this article.

2) Use DTM to Perform Calculations on the Studied System: To obtain the steady-state values of the system state variables. The key to this step is to accurately calculate each converter contained in the system one by one when simplifying all other converters using the idea of SSA in the calculation process, to reduce the complexity of the high-order system model. Therefore, this method is applicable to both the double-branch system studied in this article and the *N*-branch system with more than three parallel branches.

First, frequency transformation is required if the subconverters have different switching frequencies. Second, to reduce the computational complexity of high-order parallel systems, it is necessary to rearrange the switching modes of the subconverters.

The specific transformation and rearrangement methods can be found in Section IV-C.

DTM can be applied to all multibranch dc–dc converter systems with pulsewidth modulation (PWM) control. It is worth noting that as the number of parallel branches increases, the calculation using DTM becomes simpler compared to the traditional DMM. At the same time, due to the low coupling characteristics between the converters in the parallel system, the calculation accuracy can still be guaranteed. However, this method also has certain limitations, that is, when there is more complex coupling between subconverters, or when there are too many branches, the idea of SSA can lead to the system being overly idealized, which can result in a decrease in computational accuracy.

B. Dynamic Model of the Main Circuit and Control Circuit

In PV systems, the control circuit controls the input voltage of the dc–dc converter, not the output voltage. In practical application, the output voltage of the dc–dc converter is fixed near the local dc bus voltage through the subsequent dc–ac inverter. When studying the stability of small household PV systems, assuming that the electricity generated by PV power generation is only supplied for personal use and not fed into the power grid, the output of the dc–dc converter is directly connected to the load R_{L}. Thus, the state variable of the system can be obtained as $\boldsymbol{x} = [i_{\mathrm{L1}}\ i_{\mathrm{L2}}\ u_{\mathrm{cin1}}\ u_{\mathrm{cin2}}\ u_{\mathrm{co1}}\ u_{\mathrm{co2}}\ v_{\mathrm{c1}}\ v_{\mathrm{c2}}]^{\mathrm{T}}$, where, v_{c1} and v_{c2}, respectively, represent the integral part of the PI controller, namely$v_{\mathrm{c}i} = \int (u_{\mathrm{pv}i} - u_{\mathrm{pvref}i})\mathrm{d}t, i = 1, 2$. Applying Kirchhoff's law and substituting it into the linear Norton equivalent model of the PV generator, the differential equation can be written as follows:

$$\begin{cases} L_1 \frac{\mathrm{d}i_{\mathrm{L1}}}{\mathrm{d}t} = u_{\mathrm{pv1}} - i_{\mathrm{L1}} r_{\mathrm{L1}} - (1 - s_1)(V_{\mathrm{D1}} + U_{\mathrm{dc}}) \\ L_2 \frac{\mathrm{d}i_{\mathrm{L2}}}{\mathrm{d}t} = u_{\mathrm{pv2}} - i_{\mathrm{L2}} r_{\mathrm{L2}} - (1 - s_2)(V_{\mathrm{D2}} + U_{\mathrm{dc}}) \\ C_{\mathrm{in1}} \frac{\mathrm{d}u_{\mathrm{cin1}}}{\mathrm{d}t} = i_{\mathrm{pv1}} - i_{\mathrm{L1}} \\ C_{\mathrm{in2}} \frac{\mathrm{d}u_{\mathrm{cin2}}}{\mathrm{d}t} = i_{\mathrm{pv2}} - i_{\mathrm{L2}} \\ (1 + \frac{r_{\mathrm{co1}}}{R_L}) C_{\mathrm{o1}} \frac{\mathrm{d}u_{\mathrm{co1}}}{\mathrm{d}t} = \frac{C_{\mathrm{o1}}}{C_{\mathrm{o1}} + C_{\mathrm{o2}}} (s_1 i_{\mathrm{L1}} + s_2 i_{\mathrm{L2}} - \frac{u_{\mathrm{co1}}}{R_L}) \\ (1 + \frac{r_{\mathrm{co2}}}{R_L}) C_{\mathrm{o2}} \frac{\mathrm{d}u_{\mathrm{co2}}}{\mathrm{d}t} = \frac{C_{\mathrm{o1}}}{C_{\mathrm{o1}} + C_{\mathrm{o2}}} (s_1 i_{\mathrm{L1}} + s_2 i_{\mathrm{L2}} - \frac{u_{\mathrm{co2}}}{R_L}) \\ \frac{\mathrm{d}v_{\mathrm{c1}}}{\mathrm{d}t} = u_{\mathrm{pv1}} - u_{\mathrm{pvref1}} \\ \frac{\mathrm{d}v_{\mathrm{c2}}}{\mathrm{d}t} = u_{\mathrm{pv2}} - u_{\mathrm{pvref2}} \end{cases}. \tag{7}$$

In (7), s_1 and s_2 represent the switching modes of converter 1 and converter 2, where, $s_i = 1 (i = 1, 2)$ indicates that the switch is ON. $s_i = 0$ indicates that the switch is OFF. In addition, the output voltage of PV cells $u_{\mathrm{pv}i}$ can be converted to the input capacitor voltage $u_{\mathrm{cin}i}$ as follows:

$$u_{\mathrm{pv}i} = u_{\mathrm{cin}i} + r_{\mathrm{cin}i}(i_{\mathrm{pv}i} - i_{\mathrm{L}i}), i = 1, 2. \tag{8}$$

In (7), $i_{\mathrm{pv}i}$ can be derived by (4) and (5). According to the analysis in Section III, it can be seen that the output voltage $u_{\mathrm{pv}i}$ and the output current $i_{\mathrm{pv}i}$ of the PV cell are affected by the PV cell parameters U_{OC}, I_{SC}, U_{mpp}, and I_{mpp}, which are determined by the PV panel placement angle θ. Therefore, in subsequent analysis, the PV panel placement angle θ will become one of the key parameters to consider.

In the MPPT control loop, the error signals of input voltage $u_{\mathrm{pv}i}$ and reference voltage $u_{\mathrm{pvref}i}$ through the PI_i controller generate $u_{\mathrm{con}i}$. Compared with the sawtooth signal $u_{\mathrm{ramp}i}$, the driving pulse of the MOSFET S_i is generated. The duty cycle of converter i d_{i} can be obtained as follows:

$$K_{\mathrm{p}i}(u_{\mathrm{pv}i} - u_{\mathrm{pvref}i}) + \frac{K_{\mathrm{p}i}}{T_{ii}} \cdot v_{\mathrm{c}i} - (U_{\mathrm{L}i} + (U_{\mathrm{H}i} - U_{\mathrm{L}i})d_i) = 0. \tag{9}$$

In (9), $K_{\mathrm{p}i}$ and $T_{\mathrm{i}i}$ are the scale coefficient and integration coefficient of the PI_i controller, respectively, and $U_{\mathrm{H}i}$ and $U_{\mathrm{L}i}$ represent the peak and valley values of sawtooth wave $u_{\mathrm{ramp}i}$, respectively. In addition, in (9), when iteratively calculating the model cycle by cycle, the duty cycle d_n of the nth switching period is calculated based on the initial state variable value $\boldsymbol{x}_n$ of that switching period, which means the data required to calculate the duty cycle can be considered to remain unchanged within one switching period, as demonstrated by the zero-order holder in Fig. 2(b).

After listing the state equation and duty cycle calculation formula of the system, the dynamic model of the system can be obtained, and DTM can be used to model the studied system.

C. Simplified Discrete-Time Model of the Studied System

The traditional SSA is simple but inaccurate, while DMM is precise but difficult to apply to high-order complex systems. To speed up the calculation and ensure its accuracy, the simplified DMM for cascaded converters, which was proposed in the previous work [26] will be applied to parallel systems in this section, to model the double-branch parallel PV system. Compared with traditional methods, this method can not only maintain high calculation accuracy but also has a simpler calculation idea. Moreover, when there are converters with different switching frequencies in the system, this method can also model the system effectively. Taking the modeling of converter 1 with the duty cycle $d_1 < d_2$ as an example, the specific process of this method is shown in Fig. 6. When analyzing systems with different switching frequencies, the method can be divided into two steps:

1) Frequency Transformation: Using the idea of stroboscopic mapping, the sampling frequency is equal to the switching frequency of the system, and the data at the starting point of each switching period will be calculated in the system model. As shown in Fig. 6, when two converters have different frequencies, it is difficult to determine the specific sampling frequency by using the traditional stroboscopic mapping method. It can be seen from Fig. 6 that the working frequency and duty cycle of converter 2 before and after scaling are related as follows:

$$d_2{}' = d_2, T_2{}' = T_1. \tag{10}$$

Since duty cycle d_2 does not change before and after scaling, and scaling only takes place on the time axis, utilizing the idea of state space averaging, the basic iteration information of the state variables of converter 2 will not change significantly within one switching period. It can be seen that frequency transformation not only simplifies the calculation but also ensures the accuracy of the calculation while facilitating sampling.

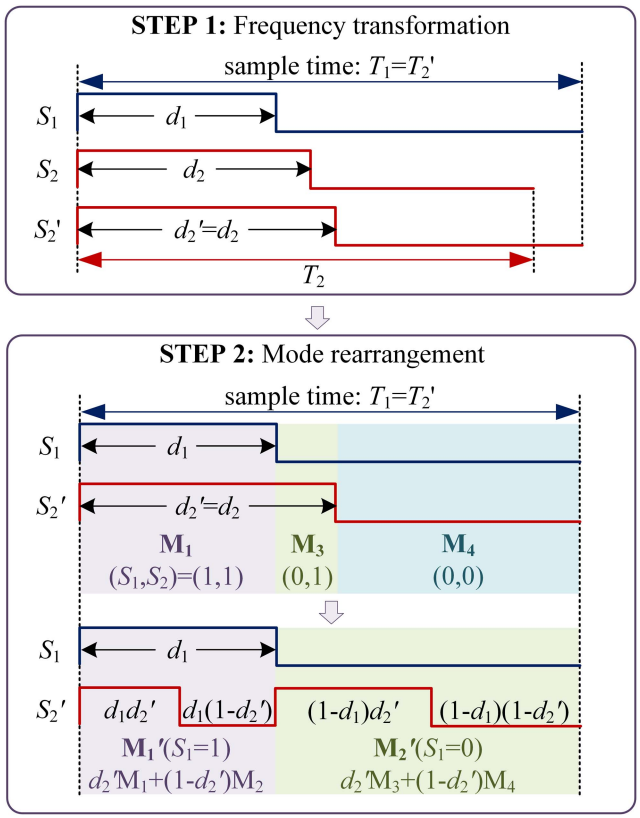

Fig. 6. Flowchart of frequency transformation and mode rearrangement ($d_1 < d_2$ as an example).

TABLE I
OPERATION MODES OF THE STUDIED SYSTEM

Mode	Switch states (s_1, s_2)	State and input matrix
M_1	(1, 1)	($\boldsymbol{A}_1$, $\boldsymbol{B}_1$)
M_2	(1, 0)	($\boldsymbol{A}_2$, $\boldsymbol{B}_2$)
M_3	(0, 1)	($\boldsymbol{A}_3$, $\boldsymbol{B}_3$)
M_4	(0, 0)	($\boldsymbol{A}_4$, $\boldsymbol{B}_4$)

2) Modal Rearrangement: It is assumed that the diode and the MOSFET are always complimentary when the continuous conduction mode is operating. In a double-branch parallel PV system, the switch has four switching modes, namely M_1 to M_4, as shown in Table I. Considering the switching mode, the system state equation can be obtained by combining (7) and (8) as

$$\dot{\boldsymbol{x}} = \boldsymbol{A}_n\boldsymbol{x} + \boldsymbol{B}_n, n= 1, 2, 3, 4. \tag{11}$$

In (9), $\boldsymbol{A}_n$ and $\boldsymbol{B}_n$ are the state matrix and input matrix in the nth switching mode, corresponding to M_1 to M_4.

For traditional DMM, it is necessary to directly list all of the possible switching forms. For the studied system, six working modes can be obtained: 1) Mode 1 ($d_2 > d_1$): When $d_2 = 1$, there are two modes in a period of the system, namely M_1 and M_3; When both d_2 and d_1 are less than 1, there are three modes, namely M_1, M_3, and M_4. 2) Mode 2 ($d_2 = d_1$): When $d_2 = d_1 = 1$, only one mode i.e., M_1, exists; When $d_2 = d_1 < 1$, there are two modes, namely M_1 and M_4. 3) Mode 3($d_2 < d_1$): When $d_1 = 1$, there are two modes, namely M_1 and M_2; When $d_1 < 1$, there are three modes, namely M_1, M_2, and M_4.

It can be seen that for high-order complex systems such as the studied system, six working modes are cumbersome. As the number of parallel branches increases, DMM will become more difficult to apply. Therefore, the method of modal rearrangement can be used to simplify the working mode of the system. Taking converter 1 as an example, the switching modes of converter 2 are rearranged. As can be seen from Table I and Fig. 6, switch s_1 of converter 1 is always on when the system operates in modes M_1 and M_2; When the system operates in modes M_3 and M_4, switch s_1 of converter 1 is always OFF. Therefore, M_1 and M_2 can be combined into switching mode M_1', M_3 and M_4 into switching mode M_2', and the corresponding coefficient matrix $\boldsymbol{A}_n$' and $\boldsymbol{B}_n$' becomes

$$\begin{cases} \boldsymbol{A}_1' = \boldsymbol{A}_1 d_2 + \boldsymbol{A}_2(1-d_2) \\ \boldsymbol{B}_1' = \boldsymbol{B}_1 d_2 + \boldsymbol{B}_2(1-d_2) \end{cases}, s_1 = 1$$

$$\begin{cases} \boldsymbol{A}_2' = \boldsymbol{A}_3 d_2 + \boldsymbol{A}_4(1-d_2) \\ \boldsymbol{B}_2' = \boldsymbol{B}_3 d_2 + \boldsymbol{B}_4(1-d_2) \end{cases}, s_1 = 0. \tag{12}$$

At this time, the working mode of the system is simplified: 1) Mode 1 ($d_1 = 1$): there is only one mode of the system in a period, namely M_1'; 2) Mode 2 ($d_1 < 1$): there are two modes, namely M_1' and M_2'. Through the above analysis, the simplified DMM of converter 1 can be obtained as follows:

$$\begin{aligned} \boldsymbol{x}_{n+1} = {} & \mathrm{e}^{\boldsymbol{A}_2'(1-d_1)T_1}\mathrm{e}^{\boldsymbol{A}_1'd_1T_1}\boldsymbol{x}_n \\ & + \mathrm{e}^{\boldsymbol{A}_2'(1-d_1)T_1}\int_{nT_1}^{nT_1+d_1T_1}\mathrm{e}^{\boldsymbol{A}_1'(nT_1+d_1T_1-\tau)}\boldsymbol{B}_1'\mathrm{d}\tau \\ & + \int_{nT_1+d_1T}^{(n+1)T_1}\mathrm{e}^{\boldsymbol{A}_2'((n+1)T_1-\tau)}\boldsymbol{B}_2'\mathrm{d}\tau. \end{aligned} \tag{13}$$

It can be seen from the above derivation that since the stroboscopic mapping is sampled only once in one period, the modal rearrangement does not change the stroboscopic sampling point. Therefore, the mode rearrangement method can not only ignore the switching process of converter 2 but also ensure that the state variable value of converter 1 will not change, that is, the accuracy of the model calculation can still be guaranteed. The simplified DMM of converter 2 can be derived by using the same steps.

To further highlight the characteristics of DTM, we comprehensively evaluate SSA, DMM, and DTM from several dimensions of computational simplicity, result accuracy, and method universality, as shown in Fig. 7. First, in terms of computational simplicity, SSA is the simplest model, while DMM is very difficult for modeling high-order systems due to the need to consider complete switch mode combinations. DTM retains the modeling steps of DMM while borrowing the ideas of SSA, resulting in computational simplicity between the two methods. Second, in terms of the accuracy of the results, SSA is the worst due to excessive idealization of the system model. At the same time, SSA can only recognize the slow-scale bifurcation. For systems with fast-scale bifurcation, using SSA is ineffective. DMM and DTM consider the switching process of the system

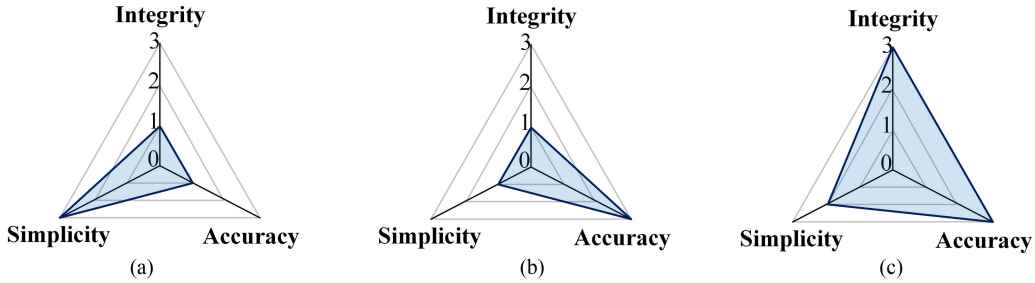

Fig. 7. Comprehensive evaluation of modeling methods. (a) SSA. (b) DMM. (c) DTM.

within one switching period, which not only improves the accuracy of the calculation results but also identifies fast and slow scale bifurcations simultaneously. Finally, in terms of method universality, traditional SSA and DMM are not only difficult to apply in high-order complex systems, but more importantly, they cannot be accurately applied to cascaded or parallel systems with different switching frequencies. The improved DTM can be well applied to multibranch converter systems in series or parallel with different switching frequencies.

It can be seen from Fig. 7 that the simplified DMM has significant effectiveness in modeling converter systems with multiple switching devices, not only has it been guaranteed in terms of computational simplicity and accuracy of results, but it can also have a wider range of applications.

Meanwhile, DTM is not only applicable to the cascaded converters studied in [26] but also to the parallel converters studied in this article. Compared to cascaded converters, the main advantage of using parallel converters is that the calculation results are more accurate and less susceptible to changes in the switching frequency. This is because compared to cascaded converters, parallel converters have a lower degree of coupling, and each converter can be connected in parallel to form a complete system or operate independently. When using DTM to model cascaded converters, the error caused by the idea of SSA will have a significant impact on the calculation results. When using DTM to model parallel converters, the error caused by this reason will be reduced.

After the simplified DMM of the parallel converter is obtained, the small signal stability of the double-branch parallel PV system can be studied by calculating the eigenvalues of the Jacobian matrix and constructing the bifurcation diagram, to judge the working state of the system and obtain the parameter boundary of the stable operation of the system.

V. Effect of Circuit Parameters on Stability

In this section, the nonlinear dynamic behaviors of the double-branch parallel PV system are analyzed by the aforementioned modeling method, and the critical parameter conditions of the converter are obtained. Finally, the accuracy of the modeling method is verified by comparison of numerical calculation and simulation when the system has different switching frequencies.

A. Nonlinear Dynamic Analysis of the Parallel PV System

In the nonlinear dynamic analysis of the converter, a series of qualitative analysis methods can be used to characterize the bifurcation and chaos of the system, to observe the stable working states of the system. Among them, bifurcation diagrams and Jacobian matrix eigenvalues as the most intuitive methods used in the analysis of this article. For example, establish the dynamic model in MATLAB and calculate and store the steady values of the inductor currents i_{L1} and i_{L2} in different bifurcation parameters to draw the bifurcation diagram.

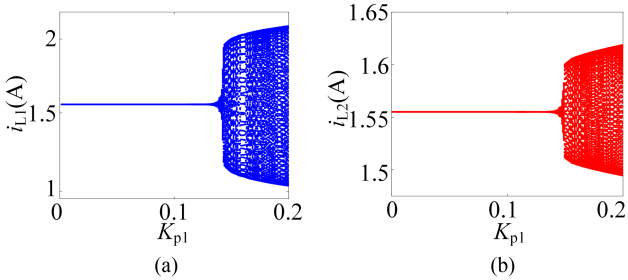

Fig. 8. Bifurcation diagram with K_{p1} as the variable. (a) Changes in the inductor current of converter 1 i_{L1}. (b) Changes in the inductor current of converter 2 i_{L2}.

Table II lists the parameters for setting a double-branch parallel PV system. To ensure the safety of the experiment, the parameters of the PV system were reduced.

1) Bifurcation When the Internal Parameters of a Single Converter Changes: When the system operates at the reference temperature $T_{ref} = 25$ °C and the reference solar irradiance $Ir_{ref} = 1000$ W/m^2, K_{p1} of PI_1 controller is taken as the bifurcation parameter, and the bifurcation of the system can be obtained as shown in Fig. 8. It can be seen from Fig. 8(a) that when $K_{p1} < 0.134$, converter 1 works stably, as K_{p1} continues to increase, Hopf bifurcation occurs in converter 1, which lead to converter 2 is also entered Hopf bifurcation as shown in Fig. 8(b). The corresponding Loci of eigenvalues are shown in Fig. 9. When the converter 1's internal parameter K_{p1} increases from 0 to 0.2, two conjugate eigenvalues of converter 1 cross the right side of the unit circle, that is, Hopf bifurcation occurs in the converter 1. At this time, the eigenvalues of converter 2 also exhibit similar trajectories, that is, Hopf bifurcation also occurs in converter 2. It can be seen that the bifurcation obtained by calculating the eigenvalues of the Jacobian matrix is consistent with that obtained from the bifurcation diagram. This further proves the mutual influence between parallel converters, that is, when a converter malfunctions due to internal parameter changes, other converters will also oscillate slightly due to output coupling.

TABLE II
PARAMETER VALUES OF MAIN CIRCUIT AND CONTROL CIRCUIT

PV arrays							
Circuit symbol	U_{OC_ref} (V)	I_{SC_ref} (A)	U_{mpp_ref} (V)	I_{mpp_ref} (A)	a	b	c
Parameter	21	1.83	18	1.66	0.102	-0.36099	0.3
Main circuit and control circuit							
Circuit symbol	C_{in1}, C_{in2} (uF)	r_{cin1}, r_{cin2}(Ω)	C_{o1}, C_{o2} (uF)	r_{co1}, r_{co2}(Ω)	L_1, L_2 (mH)	r_{L1}, r_{L2} (Ω)	V_{D1}, V_{D2}(V)
Parameter	100	0.04	100	0.04	2	0.8	0.55
Circuit symbol	K_{p1}	K_{p2}	T_{i1}	T_{i2}	f_{s1} (kHz)	f_{s2} (kHz)	R_L(Ω)
Parameter	(0.0001, 0.2)	0.05	0.0015	0.0015	20	20	20

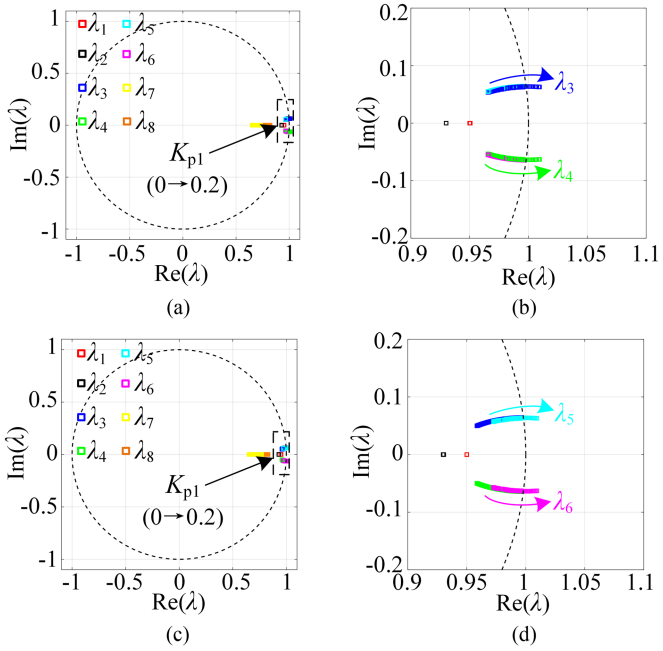

Fig. 9. Loci of eigenvalues. (a) Converter 1 when K_{p1} from 0 to 0.2. (b) Enlarged view of (a). (c) Converter 2 when K_{p1} from 0 to 0.2. (d) Enlarged view of (c).

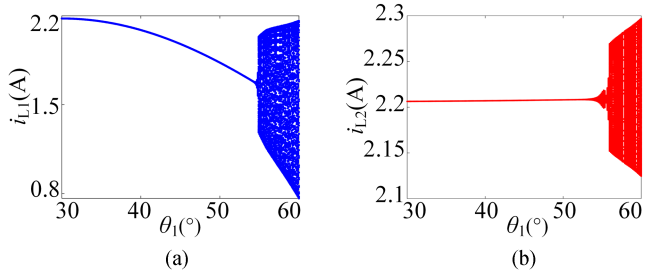

Fig. 10. Bifurcation diagram with θ_1 as the variable. (a) Changes in the inductor current of converter 1 i_{L1}. (b) Changes in the inductor current of converter 2 i_{L2}.

Hopf bifurcation generated by increasing K_{p1} belongs to slow-scale bifurcation. The reason why fast-scale bifurcations were not identified is due to the control method of the converter. In general, if the control method is peak current control, the duty cycle of the power device is greater than 50%, which will cause the system to generate subharmonic oscillations, that is, the state variable will be identified as a period-doubling bifurcation. The voltage control method used in this article does not have subharmonic oscillation, and usually only slow-scale bifurcation phenomena such as Hopf bifurcation.

2) Bifurcation When the Placement Angle of PV Panels Changes: When the system operates at the reference temperature $T_{ref} = 25\,^{\circ}$C, the vertical plane solar irradiance $Ir_T = 1600$ W/m^2 and the PI$_1$ controller parameters are $(K_p, T_i) = (0.10.001)$. Set the PV panel placement of converter 2 $\theta_2 = 30°$, and the PV panel placement of converter 1 θ_1 as the bifurcation parameter. It can be seen from Fig. 10(a), when the placement angle of PV 1 $\theta_1 < 52.4°$, the inductor current i_{L1} of converter 1 decreases with the increase of placement angle θ_1 but always maintains stable operation. Continue to increase the placement angle θ_1 of PV 1, when $\theta_1 = 52.4°$, Hopf bifurcation occurs in converter 1. It can be seen from Fig. 10(b) that the change in the placement angle of PV panel 1 also has a slight impact on the stability of converter 2. When the placement angle of PV panel 1 $\theta_1 < 52.4°$, as converter 1 is in a stable working state of period 1 and the placement angle θ_2 of PV panel 2 has not changed, converter 2 always operates stably and the value of inductor current i_{L2} does not change. Continuing to increase the placement angle θ_1, converter 2 also enters a slight Hopf bifurcation. The same change rule can be obtained from the motion trajectories of eigenvalues in Fig. 11. It can be seen that the placement angle of PV panels will not only affect the output power of PV generators but also affect the stability of the system operation.

B. Stability Boundary of Circuit Parameters

Based on this model, the stability region of the entire system is divided when the parameters of converter 1 change. From the above analysis, it can be seen that changes in the parameters of converter 1 will have a slight impact on the stability of converter 2. Therefore, using K_{p1}–θ_1 as the coordinate observation point, the stability region of the system can be obtained as shown in Fig. 12. It can be seen from Fig. 12 that the larger the proportion coefficient K_{p1}, the more unstable the system is, and the placement angle θ_1 of the PV 1 is the same. The above instability is caused by Hopf bifurcation.

Based on the above analysis, we can pay attention to the following points when designing the parameters of the PV system.

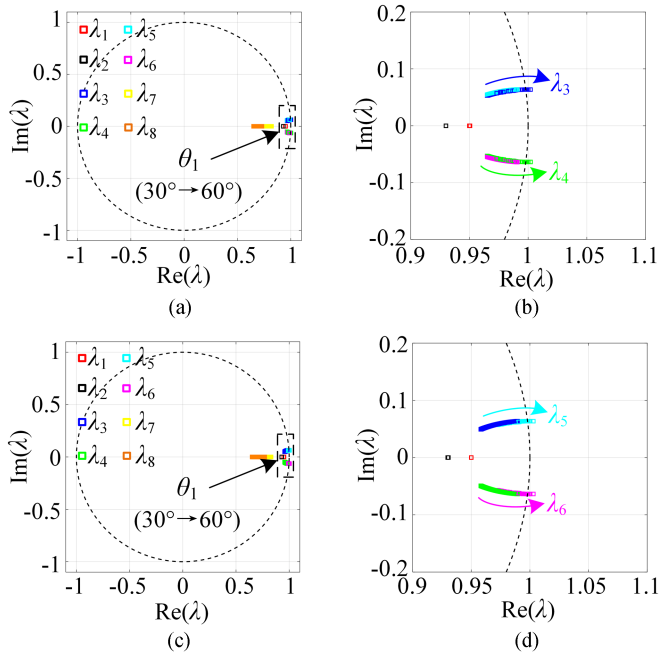

Fig. 11. Loci of eigenvalues. (a) Converter 1 when θ_1 from 30° to 60°. (b) Enlarged view of (a). (c) Converter 2 when θ_1 from 30° to 60°. (d) Enlarged view of (c).

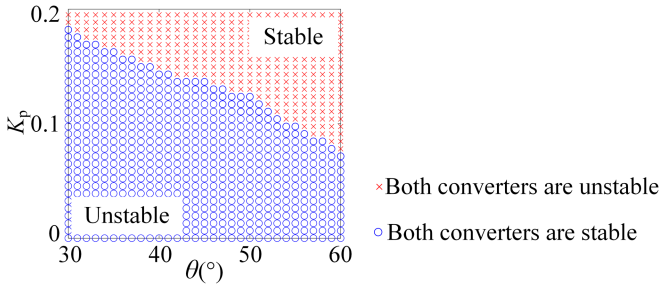

Fig. 12. Stability region.

1) The parameters of the PI controller inside the converter should choose the relatively small K_{p1}.
2) When the solar irradiance is constant, the placement angle between the PV panel and the horizontal plane should be as small as possible to ensure that the system absorbs enough solar energy.
3) When selecting the site of the system, it is also necessary to comprehensively consider the influence of geographical factors such as local altitude and latitude on the actual solar irradiance received by the system, that is, to ensure that the system receives the maximum solar irradiance as far as possible.

C. Influence of Frequency Difference on Model Accuracy

This section will discuss the accuracy of applying the model to different frequency systems. By changing the switching frequency f_{s2} of converter 2, the errors can be obtained, as shown in Figs. 13 and 14.

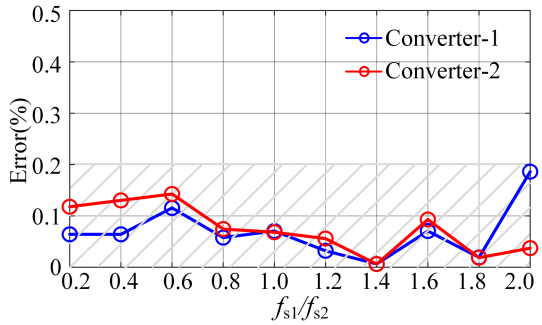

Fig. 13. Error of steady value varying with switching frequency.

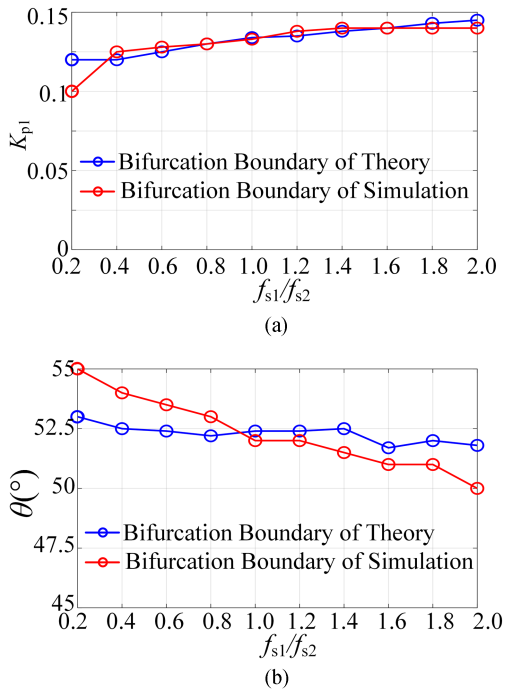

Fig. 14. Error of bifurcation boundary varying with switching frequency. (a) K_{p1} as the variable. (b) θ_1 as the variable.

1) Error of Steady Value: Set the system to work with the reference temperature $T_{ref} = 25\,^{\circ}\mathrm{C}$ and reference solar irradiance $Ir_{ref} = 1000\ \mathrm{W/m^2}$. When the switching frequency f_{s1} of converter 1 is fixed as 20 kHz and the switching frequency of converter 2 is changed from $0.2f_{s1}$ to $2f_{s1}$, the theoretical and simulation values of the steady-state of the system can be obtained as shown in Table III.

By comparing theoretical and simulated values with data provided in Table III, the steady-state error of the system can be obtained by using the following formula:

$$\text{error} = \left| \frac{i_{\text{Li\_theory}} - i_{\text{Li\_real}}}{i_{\text{Li\_real}}} \right|. \tag{14}$$

The calculation results are shown in Fig. 13. It can be seen that the calculation accuracy of the theoretical method is very high, and the error remains below 0.2%, which further proves the effectiveness of the model established in this article.

TABLE III
ERROR IN DIFFERENT SWITCHING FREQUENCY

f_{s2}/f_{s1}	i_{L1_theory}(A)	i_{L1_real}(A)	i_{L2_theory}(A)	i_{L2_real}(A)
0.2	1.5561	1.5571	1.1363	1.1382
0.4	1.5561	1.5571	1.3962	1.3983
0.6	1.5561	1.5579	1.4833	1.4856
0.8	1.5561	1.5570	1.5365	1.5377
1.0	1.5561	1.5572	1.5561	1.5572
1.2	1.5561	1.5566	1.5701	1.5692
1.4	1.5561	1.5562	1.5849	1.5848
1.6	1.5561	1.5550	1.5923	1.5938
1.8	1.5561	1.5564	1.6038	1.6041
2.0	1.5561	1.5532	1.6124	1.6118

2) Error of Bifurcation Boundary: First, set the system to work with the reference temperature $T_{\rm ref} = 25\,^{\circ}$C and reference solar irradiance $Ir_{\rm ref} = 1000$ W/m^2. When changing the switching frequency f_{s2} with K_{p1} as the bifurcation parameter, the bifurcation boundary error of the system is shown in Fig. 14(a). It can be seen that the change in switching frequency does not have a significant impact on the bifurcation boundary, and there is no significant error between theory and simulation.

Second, K_{p1} is set to 0.1 and the rest of the parameters are consistent with Table II. At the PV panel placement angle θ_1 is the bifurcation parameter, and changing the switching frequency f_{s2}, the bifurcation boundary error can be obtained, as shown in Fig. 14(b). It can be seen that the change in switching frequency has little impact on bifurcation boundaries. However, the bifurcation boundaries obtained from theoretical calculations and simulations still have certain errors, mainly due to the difference between the theoretical calculation method and simulation calculation method of PV generators in Section III. However, for the need for linear equivalence of the output characteristic curve of the PV generator, the engineering equivalent mathematical model is mainly considered in this article.

Overall, DTM is suitable for modeling multibranch parallel converters. Meanwhile, in our previous work [26], the cascaded converters could only control the model error to around 5%, and the error would also increase as the switching frequency difference increased. However, this problem did not occur due to the low coupling of parallel converters. Therefore, DTM has higher accuracy when applied to parallel converters.

VI. EXPERIMENTAL VALIDATION

A prototype of a double-branch parallel PV system, as shown in Fig. 15, was designed to study and verify the nonlinear behaviors analyzed in the previous sections. The parameters of the prototype used are the same as those in Table II. For the power circuit, the input terminals of the two converters are respectively powered by Chroma 62150H-1000S dc power supply and IT6006C-500-40 dc power supply, to simulate the PV array. The output terminals are connected to the same load. The control loop is implemented by a Digital Signal Processor (DSP TMS320F28335): First, voltage dividing resistors and an

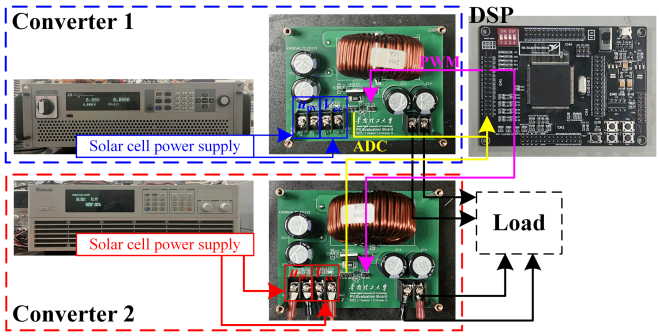

Fig. 15. Photo of the experimental circuit.

operational amplifier (TLV271) are used to sample the PV output voltage $u_{\rm pv}$. Then, the sampled signal is input into the ADC port of the DSP, and the logic of the control loop is implemented through the DSP. The correct PWM signal is output from the ePWM port of the DSP, and then driven by the driving chip (UCC27517) to turn ON and OFF the MOSFET. Ultimately, the output of the PV array is maintained near the maximum power point. Observing the waveforms of the inductor current output from the prototype, the nonlinear behaviors consistent with the theoretical results analyzed in Section V can be obtained.

A. Verifying the Impact of Internal Parameter Changes on System Stability

i_{L1} and i_{L2} waveforms of the system are shown in Fig. 16, in which the internal parameters of a single converter change, and set the reference temperature $T_{\rm ref} = 25\,^{\circ}$C and the reference solar irradiance $Ir_{\rm ref} = 1000$ W/m^2. Set the gain K_{p1} of the PI controller in converter 1 to 0.05, the system can maintain stable operation in the state of period 1, as shown in Fig. 16(a). Increase K_{p1} to 0.13, which is located near the bifurcation boundary. A slight oscillation of the inductor current i_{L1} can be observed, as shown in the green waveform in Fig. 16(b). At this point, due to the output terminal being connected to the same load, the two converters are coupled to each other. So, converter 2 also undergoes Hopf bifurcation. That is, a slight oscillation of the inductor current i_{L2} is observed, as shown in the magenta waveform in Fig. 16(b). Set K_{p1} to 0.2, it is observed in the experiment that the inductor current i_{L1} and i_{L2} experience a more severe low-frequency oscillation, as shown in Fig. 16(c).

B. Verifying the Impact of External Condition Changes on System Stability

The actual received solar irradiance of a single PV power source changes, and set $K_{p1} = 0.1$, the obtained waveforms of i_{L1} and i_{L2} are shown in Fig. 17. When the solar irradiance $Ir_{\rm T} = 1600$ W/m^2 and both PV panels placement angle θ are 30°, the system can maintain stable operation in period 1, as shown in Fig. 17(a). When the placement angle of converter 1 θ_1 is set to 50°, the actual received solar irradiance of PV panel 1 decreases, inductor current i_{L1} is decreased, and the slight oscillation of the inductor currents i_{L1} and i_{L2} can be observed, as shown in Fig. 17(b). Increase θ_1 to 60°, a more severe low-frequency oscillation is observed, as shown in the

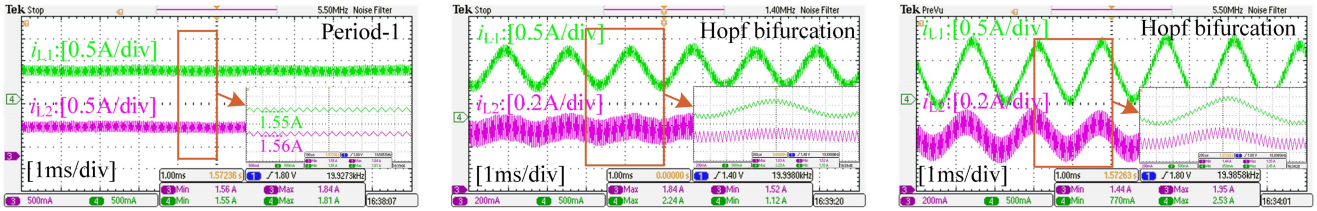

(a) (b) (c)

Fig. 16. Experimental results with K_{p1} as the variable. (a) $K_{p1} = 0.05$. (b) $K_{p1} = 0.13$. (c) $K_{p1} = 0.2$.

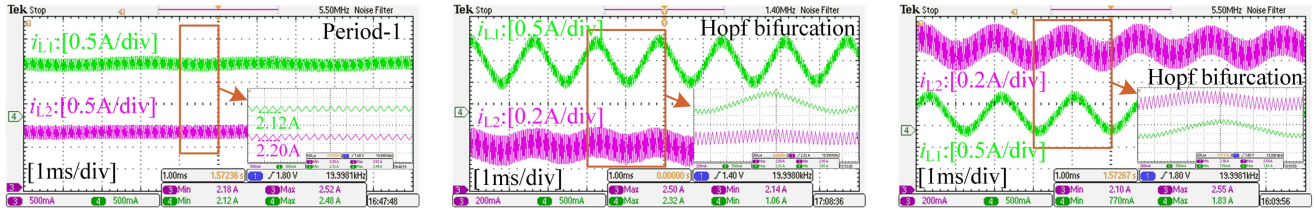

(a) (b) (c)

Fig. 17. Experimental results with θ_1 as the variable. (a) $\theta_1 = 30°$. (b) $\theta_1 = 50°$. (c) $\theta_1 = 60°$.

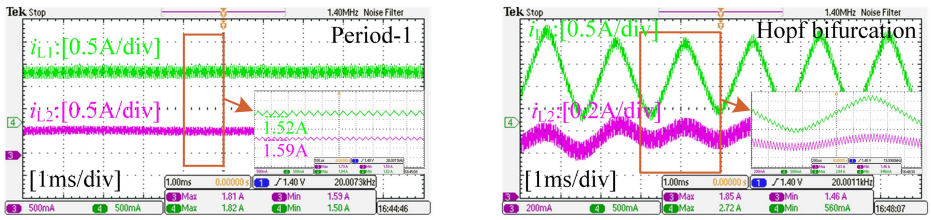

(a) (b)

Fig. 18. Experimental results with K_{p1} as the variable ($f_{s1} = 20$ kHz, $f_{s2} = 28$ kHz). (a) $K_{p1} = 0.05$. (b) $K_{p1} = 0.2$.

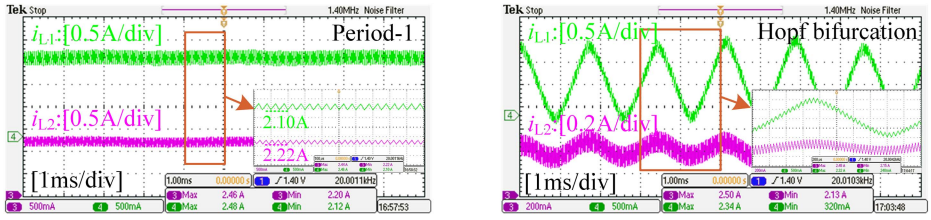

(a) (b)

Fig. 19. Experimental results with θ_1 as the variable ($f_{s1} = 20$ kHz, $f_{s2} = 28$ kHz). (a) $\theta_1 = 30°$. (b) $\theta_1 = 60°$.

green waveform in Fig. 17(c). Although there are no changes in the parameters in converter 2, converter 2 also undergoes Hopf bifurcation due to the coupling at the output end. Where, a slight oscillation of the inductor current i_{L2} is observed, as shown in the magenta waveform in Fig. 17(c).

C. Verifying the System Stability When the Switching Frequency Changes

First, keep other parameters unchanged and increase the switching frequency of converter 2f_{s2} to 28 kHz. At this time, when K_{p1} is also set to 0.05, the system works stably in the working state of period 1, as shown in Fig. 18(a). it can also be seen that the steady-state values of the inductor currents obtained from the experiment are $i_{L1} = 1.52$ A and $i_{L2} = 1.59$ A, which are almost consistent with the theoretical calculation values, further verifying the accuracy of the studied model. When increasing K_{p1} to 0.2, the system occurs Hopf bifurcation, as shown in Fig. 18(b). Similarly, when $f_{s2} = 28$ kHz and $\theta_1 = 30°$ or 60°, stable and Hopf bifurcations consistent with theoretical analysis can be observed, as shown in Fig. 19.

The excellent agreement between the theoretical analysis and experimental results verifies the accuracy of the simplified DTM in analyzing nonlinear behaviors in parallel systems.

VII. Conclusion and Future Plans

Due to the intermittency of renewable energy systems, dc distribution systems are usually designed in the form of multiple parallel branches to improve system reliability. In this article, for the presence of multiple switching modes and multiple state variables in parallel converters, a simplified DTM is used to model a double-branch parallel PV system, and its nonlinear behavior is analyzed. In future designs, for the circuit using voltage mode control with PI controller, the excessive gain of PI controller K_{p} can cause system oscillations. Moreover, for the circuit where the PV generator serves as the input power source, the placement angle of the PV panel directly affects the maximum power point voltage and current. When the placement angle of the PV panel increases, the output current of the PV generator will decrease, that is, the inductor current of the converter will also decrease. When the placement angle of the PV panel is too large, the circuit will oscillate.

In addition, DTM used in this article can be applicable to all PWM-controlled multibranch converter systems. In future work, the proposed model can be applied to different energy storage systems with more practical value in dc distribution systems, to avoid special nonlinear behaviors caused by unreasonable parameters in system design. For the modeling of parallel systems such as new energy generation systems, which are highly susceptible to external conditions, the mathematical model is established in this article has significant effects in terms of accuracy, rapidity, and simplicity.

However, this article also has certain limitations. In terms of the uncertainty of the constructed model, when applying it to other systems in the future, the following factors need to be considered.

1) The deviation between the new energy power supply model and the actual model.
2) Errors caused by parasitic parameters in circuits.
3) For other complex systems with higher coupling, such as cascaded converters with higher coupling than parallel converters, the idea of SSA will bring certain errors to the modeling results.

In future work, a more comprehensive and simpler model still needs to be proposed, to minimize the impact of model uncertainty as much as possible.

References

[1] S. Kouro, J. I. Leon, D. Vinnikov, and L. G. Franquelo, "Grid-connected photovoltaic systems: An overview of recent research and emerging PV converter technology," *IEEE Ind. Electron. Mag.*, vol. 9, no. 1, pp. 47–61, Mar. 2015, doi: 10.1109/MIE.2014.2376976.

[2] H. D. Tafti, C. D. Townsend, G. Konstantinou, and J. Pou, "A multi-mode flexible power point tracking algorithm for photovoltaic power plants," *IEEE Trans. Power Electron.*, vol. 34, no. 6, pp. 5038–5042, Jun. 2019, doi: 10.1109/TPEL.2018.2883320.

[3] D. Lin, X. Li, S. Ding, and Y. Du, "Strategy comparison of power ramp rate control for photovoltaic systems," *CPSS Trans. Power Electron. Appl.*, vol. 5, no. 4, pp. 329–341, Dec. 2020, doi: 10.24295/CPSSTPEA.2020.00027.

[4] A. El Aroudi, M. Al-Numay, G. Garcia, K. Al Hossani, N. Al Sayari, and A. Cid-Pastor, "Analysis of nonlinear dynamics of a quadratic boost converter used for maximum power point tracking in a grid-interlinked PV system," *Energies*, vol. 12, no. 1, 2019, Art. no. 61.

[5] C. M. F. S. Reza and D. D.-C. Lu, "Recent progress and future research direction of nonlinear dynamics and bifurcation analysis of grid-connected power converter circuits and systems," *IEEE J. Emerg. Sel. Topics Power Electron.*, vol. 8, no. 4, pp. 3193–3203, Dec. 2020, doi: 10.1109/JESTPE.2019.2961713.

[6] X. Xiong and X. Ruan, "Non-smooth bifurcation analysis of multi-structure multi-operating-mode power electronics systems for applications with renewable energy sources," *IEEE Trans. Circuits Syst. II, Exp. Briefs*, vol. 66, no. 3, pp. 487–491, Mar. 2019, doi: 10.1109/TCSII.2018.2863690.

[7] M. K. Zadeh, R. Gavagsaz-Ghoachani, J. P. Martin, S. Pierfederici, B. Nahid-Mobarakeh, and M. Molinas, "Discrete-time tool for stability analysis of dc power electronics-based cascaded systems," *IEEE Trans. Power Electron.*, vol. 32, no. 1, pp. 652–667, Jan. 2017.

[8] W. Li and X. He, "Review of nonisolated high-step-up dc/dc converters in photovoltaic grid-connected applications," *IEEE Trans. Ind. Electron.*, vol. 58, no. 4, pp. 1239–1250, Apr. 2011.

[9] Y. Murakawa and T. Hikihara, "Output series-parallel connection of passivity-based controlled dc–dc converters: Generalization of asymptotic stability," *IEEE Trans. Circuits Syst. I, Reg. Papers*, vol. 68, no. 4, pp. 1750–1759, Apr. 2021, doi: 10.1109/TCSI.2021.3054932.

[10] Y. Xia, M. Yu, Y. Peng, and W. Wei, "Modeling and analysis of circulating currents among input-parallel output-parallel nonisolated converters," *IEEE Trans. Power Electron.*, vol. 33, no. 10, pp. 8412–8426, Oct. 2018, doi: 10.1109/TPEL.2017.2777604.

[11] M. M. Shebani, T. Iqbal, and J. E. Quaicoe, "Synchronous switching for parallel-connected dc-dc B converters," in *Proc. IEEE Elect. Power Energy Conf.*, 2017, pp. 1–6, doi: 10.1109/EPEC.2017.8286189.

[12] M. Huang, H. Ji, J. Sun, L. Wei, and X. Zha, "Bifurcation-based stability analysis of photovoltaic-battery hybrid power system," *IEEE J. Emerg. Sel. Topics Power Electron.*, vol. 5, no. 3, pp. 1055–1067, Sep. 2017.

[13] P. Shaw, "Modelling and analysis of an analogue MPPT-based PV battery charging system utilising dc–dc boost converter," *IET Renewable Power Gener.*, vol. 13, pp. 1958–1967, 2019.

[14] D. Chen, H. Ji, Y. Liu, and X. Zha, "Large signal modeling and stability analysis of photovoltaic-battery hybrid power system," in *Proc. IEEE Energy Convers. Congr. Expo.*, 2018, pp. 4168–4172, doi: 10.1109/ECCE.2018.8557916.

[15] A. Bandyopadhyay and S. Parui, "Bifurcation behavior of photovoltaic panel fed Cuk converter connected to different types of loads," in *Proc. Int. Symp. Devices, Circuits Syst.*, 2018, pp. 1–5, doi: 10.1109/ISDCS.2018.8379671.

[16] X. Xiong and Y. Yang, "A photovoltaic-based dc microgrid system: Analysis, design and experimental results," *Electronics*, vol. 9, no. 6, 2020, Art. no. 941.

[17] X. Xiong, C. K. Tse, and X. Ruan, "Bifurcation analysis of standalone photovoltaic-battery hybrid power system," *IEEE Trans. Circuits Syst. I, Reg. Papers*, vol. 60, no. 5, pp. 1354–1365, May 2013, doi: 10.1109/TCSI.2013.2239140.

[18] X. Xiong, C. K. Tse, and X. Ruan, "Bifurcation analysis and experimental study of a multi-operating-mode photovoltaic-battery hybrid power system," *IEEE J. Emerg. Sel. Topics Circuits Syst.*, vol. 5, no. 3, pp. 316–325, Sep. 2015, doi: 10.1109/JETCAS.2015.2462015.

[19] K. F. Krommydas and A. T. Alexandridis, "Nonlinear analysis methods applied on grid-connected photovoltaic systems driven by power electronic converters," *IEEE J. Emerg. Sel. Topics Power Electron.*, vol. 8, no. 4, pp. 3293–3306, Dec. 2020, doi: 10.1109/JESTPE.2020.2992969.

[20] D. Peng, M. Huang, J. Li, J. Sun, X. Zha, and C. Wang, "Large-signal stability criterion for parallel-connected dc–dc converters with current source equivalence," *IEEE Trans. Circuits Syst. II, Exp. Briefs*, vol. 66, no. 12, pp. 2037–2041, Dec. 2019, doi: 10.1109/TCSII.2019.2895842.

[21] H. Li et al., "An extended stability analysis method for paralleled dc-dc converters system with considering the periodic disturbance based on Floquet theory," *IEEE Access*, vol. 8, pp. 9023–9036, 2020.

[22] L. Ding, S. C. Wong, and C. K. Tse, "Bifurcation analysis of a current mode-controlled dc cascaded system and applications to design," *IEEE J. Emerg. Sel. Topics Power Electron.*, vol. 8, no. 4, pp. 3214–3224, Dec. 2020.

[23] H. Li, J. Shang, B. Zhang, X. Zhao, N. Tan, and C. Liu, "Stability analysis with considering the transition interval for PWM dc-dc converters based on describing function method," *IEEE Access*, vol. 6, pp. 48113–48124, 2018, doi: 10.1109/ACCESS.2018.2857846.

[24] H. Li, Z. Zhang, Z. Zhou, Z. Chu, Y. Zeng, and Z. Qiu, "A Floquet theory-based stability analysis method for cascaded dc-dc converters by combining with the describing function of PWM link," in *Proc. IEEE Energy Convers. Congr. Expo.*, 2021, pp. 2841–2846.
[25] H. Ji, F. Xie, Y. Chen, and B. Zhang, "Small-step discretization method for modeling and stability analysis of cascaded dc–dc converters with considering different switching frequencies," *IEEE Trans. Power Electron.*, vol. 37, no. 8, pp. 8855–8872, Aug. 2022.
[26] C. Cheng, F. Xie, B. Zhang, D. Qiu, W. Xiao, and H. Ji, "Modeling and nonlinear dynamic analysis of cascaded dc–dc converter systems based on simplified discrete mapping," *IEEE Trans. Ind. Electron.*, vol. 70, no. 6, pp. 5830–5839, Jun. 2023, doi: 10.1109/TIE.2022.3192684.
[27] B. N. Alajmi, K. H. Ahmed, S. J. Finney, and B. W. Williams, "A maximum power point tracking technique for partially shaded photovoltaic systems in microgrids," *IEEE Trans. Ind. Electron.*, vol. 60, no. 4, pp. 1596–1606, Apr. 2013.
[28] E. M. G. Rodrigues, R. Godina, M. Marzband, and E. Pouresmaeil, "Simulation and comparison of mathematical models of PV cells with growing levels of complexity," *Energies*, vol. 11, 2018, Art. no. 2902.
[29] P. Zhang, "Research on accurate engineering mathematical model of PV cells and simulation characteristics," *Trans. Elect. Electron. Mater.*, vol. 22, pp. 167–176, 2021.
[30] S. R. Fahim, H. M. Hasanien, R. A. Turky, S. H. E. A. Aleem, and M. Ćalasan, "A comprehensive review of photovoltaic modules models and algorithms used in parameter extraction," *Energies*, vol. 15, 2022, Art. no. 8941.
[31] S. M. Hassan Hosseini and A. A. Keymanesh, "Design and construction of photovoltaic simulator based on dual-diode model," *Sol. Energy*, vol. 137, pp. 594–607, 2026, doi: 10.1016/j.solener.2016.09.001.
[32] A. S. Ahmad, "Parameters estimation of photovoltaic cells using simple and efficient mathematical models," *Sol. Energy*, vol. 209, pp. 245–257, 2020.
[33] C. Fang et al., "Stability analysis of photovoltaic and battery energy storage systems integrated to weak grid," in *Proc. IEEE 3rd Int. Conf. Electron. Technol.*, 2020, pp. 480–484, doi: 10.1109/ICET49382.2020.9119516.
[34] L. Guo, L. Xu, K. Sun, and Y. Li, "Stability analysis of standalone photovoltaic system considering controller time delay," in *Proc. IEEE 4th Conf. Energy Internet Energy Syst. Integr.*, 2020, pp. 57–62, doi: 10.1109/EI250167.2020.9347340.
[35] S. Liu, P. X. Liu, and X. Wang, "Stochastic small-signal stability analysis of grid-connected photovoltaic systems," *IEEE Trans. Ind. Electron.*, vol. 63, no. 2, pp. 1027–1038, Feb. 2016, doi: 10.1109/TIE.2015.2481359.
[36] Y. Guo, F. Tang, X. Wei, J. Xie, J. Qi, and Z. Liu, "Small-signal stability modeling and analysis of power system with integrated photovoltaic energy storage," in *Proc. IEEE 6th Conf. Energy Internet Energy Syst. Integr.*, 2022, pp. 2850–2856.
[37] Y. Xu and Z. Gu, "Stability analysis and control of two-stage three-phase photovoltaic grid-connected system with phase-locked loop," in *Proc. 2nd IEEE Conf. Energy Internet Energy Syst. Integr.*, 2018, pp. 1–6.

Xinyue Geng was born in Yunnan, China, in 2000. She received the B.S. degree in electrical engineering and automation in 2021 from South China University of Technology, Guangzhou, China, where she is currently working toward the M.S. degree in power electronics.

Her research interests include the modeling method, stability, and nonlinear behavior analysis of power electronics systems.

Bo Zhang (Fellow, IEEE) was born in Shanghai, China, in 1962. He received the B.S. degree in electrical engineering from Zhejiang University, Hangzhou, China, in 1982, the M.S. degree in power electronics from Southwest Jiaotong University, Chengdu, China, in 1988, and the Ph.D. degree in power electronics from Nanjing University of Aeronautics and Astronautics, Nanjing, China, in 1994.

He is currently a Professor with the School of Electric Power, South China University of Technology, Guangzhou, China. He has authored or coauthored six books in IEEE-Wiley and Springer, two books in Science Press in China, and more than 450 technical papers, and holds 100 patents. His research interests include nonlinear analysis, modeling and control of power electronic converters, and wireless power transfer applications.

Dongyuan Qiu (Senior Member, IEEE) was born in China in 1972. She received the B.S. and M.S. degrees in automation from the South China University of Technology, Guangzhou, China, in 1994 and 1997, respectively, and the Ph.D. degree in electronic engineering from the City University of Hong Kong, Hong Kong, in 2002.

She is currently a Professor with the School of Electric Power, South China University of Technology. She has authored or coauthored three books and more than 200 papers and holds about 100 patents. Her research interests include modeling of power electronic converters, wireless power transfer, and fault diagnosis.

Dr. Qiu is an Associate Editor for IEEE TRANSACTIONS ON POWER ELECTRONICS

Yanfeng Chen (Member, IEEE) received the M.S. degree in power electronics technology from Wuhan University, Wuhan, China, in 1995, and the Ph.D. degree in circuits and systems from South China University of Technology, Guangzhou, China, in 2000.

From 2005 to 2006, she was a Research Associate with the Department of Electronic and Information Engineering, Hong Kong Polytechnic University, Hong Kong. She is currently a Professor with the School of Electric Power, South China University of Technology. She authored or coauthored three books and more than 50 papers and holds 50 patents. Her research interests include modeling and analysis of nonlinear systems and power electronics.

Wenxun Xiao (Member, IEEE) was born in Hainan, China, in 1979. He received the B.S. degree in electrical engineering and automation and the M.S. and Ph.D. degrees in power electronics and power drives from the South China University of Technology, Guangzhou, China, in 2002, 2005, and 2008, respectively.

Since 2008, he has been with the School of Electrical Power, South China University of Technology, where he is currently an Associate Professor. His research interests include topologies and control methods of power electronics, wireless power transmission technology, renewable energy technologies, and microgrids.

Fan Xie (Member, IEEE) received the B.S. and M.S. degrees in physics and physical electronics from the School of Physics and Electron Engineering, Guangzhou University, Guangzhou, China, in 2008 and 2011, respectively, and the Ph.D. degree in power electronics from South China University of Technology, Guangzhou, China, in 2014.

In 2014, he joined the School of Electric Power, South China University of Technology, where he has been an Associate Professor since 2018. His research interests include nonlinear dynamics of power electronic circuits and control of power supplies and ac drives.